Factors controlling segregation tendency of solute Ti, Ag and Ta into different symmetrical tilt grain boundaries of tungsten: First-principles and experimental study

Ahmed Tamer AlMotasem[a,b], Teodor Huminiuc[a] and Tomas Polcar[a]

[a)] *Engineering Materials, Department of Mechanical Engineering, University of Southampton, Southampton, SO17 1BJ, UK*

[b)] *Physics Department, Faculty of Science, Assiut University, Assiut, 71516, Egypt*

Abstract

In previous reports, experimental studies have shown that both thermal stability and strength can be controlled by grain boundary (GB) segregation. In this study, we investigate the segregation behavior of solute (Ti, Ag and Ta) atoms to low/high-angle symmetric tilt grain boundaries (STGBs) of W using density functional theory (DFT) calculations and supported by TEM experiments. We found no segregation preference for Ti or Ta at low-angle STGBs; however, they exhibit a slight segregation tendency to the core of high-angle STGBs. In contrast, Ag is more prone to segregate in and all around the GB plane. We estimated the mechanical and electronic contributions to solution energy and found that the electronic contribution is dominant. Furthermore, the role of $d-$ valence electrons of solute and W atoms, was analyzed using the local density of states (PDOS). We found that substantial $d-$ valence electrons hybridization in the case of Ta plays an important role in stabilizing W-Ta bonds, while the anisotropic nature of W-Ti bond contributes to ~~stabilize~~ stabilizing surrounding W atoms. Charge transfer analysis revealed that Ti and Ta lose electrons to W atoms. Contrary to the electronegativity rule, Ag atoms gain charge from neighboring W atoms and excellent $s-s$ hybridization may explain the increased GB segregation of Ag atoms.

Keywords: Ti/Ag/Ta segregation, Grain boundaries, Tungsten, First-principles calculations, Transmission electron microscopy (TEM)

*Corresponding Author: Ahmed Tamer AlMotasem (a.almotasem@aun.edu.eg)

1. Introduction

Tungsten possesses a set of unique metallic properties such as the highest melting point, high elastic modulus, high density, high thermal conductivity, and excellent mechanical strength[1,2]. Hence, W-based alloys are known to be promising candidates for a wide range of technological and industrial applications. They are the primary choice for filaments, heating elements, and kinetic energy penetrators. However, a major drawback of elemental W is low ductility and high ductile-to-brittle-transition temperature (DBTT) above room temperature which limits their use in harsh environments [3]. Improving the mechanical properties of tungsten alloys could have a significant impact on manufacturing and broadening the range of applications for the resulting materials. Different strategies have been proposed to achieve higher levels of strength, such as solid solution and grain boundary (GB) solute segregation. In the literature, there is an abundance of experimental and theoretical studies focused on enhancing the thermal stability of single metal by alloying. In previous pioneering works [4–8], it is reported that substantially improved thermal stability of binary nanocrystalline alloys could be achieved by elemental segregation at GBs. It has been shown that GB segregation of solute elements can alter the mechanical properties of the material due to either weaken or strengthen the grain boundaries [9–13]. With respect to thermal stability, Donaldson *et al.*[14], reported that the abnormal growth of W can be significantly reduced by alloying with Ti and they attributed such behavior to the Ti segregation to the grain boundary. Recently, Callisti *et al*. [15] showed that for W-Ti alloys, the microstructure observed at 923 K remained stable upon cooling to room temperature and consisted of Ti-rich regions along the columnar grain boundaries and of alternate Ti-rich and Ti-depleted nanoscale domains in the interior of the grains, which formed a stable dual-phase nanocrystalline structure. Besides, DFT results [16,17] confirm that Ta and Ti are fully soluble in W and the addition of these two elements to

the solid solution led to significant enhancement of the thermal stability and mechanical properties of W.

Moreover, Wu *et al* [18] investigated the segregation behavior of (Sr, Th, In, Cd, Ag, Sc, Au, Zn, Cu, Mn, Cr, and Ti) in symmetric tilt grain boundary Σ3 (111) [110] in W. It was concluded that the alloying atom, with larger metal radius than W, acts as an embrittler and for those with smaller metal radii act as cohesion enhancer. In a similar piece of work, X. Wu et al [19] investigate the effect of GBs morphology and substituent radii on the segregation behavior in symmetrical tilt grain boundaries of tungsten. They found that GB strengthening by solute segregation depends strongly on the GB structures. Additionally, their results showed that solutes with larger(smaller) radii tend to strengthen (weaken) grain boundary in W.

More recently, Scheiber *et al.*[20] have explored the effect of all transition metals (TM) segregants on the strength and cohesion of GB of W. They reported that strengthening elements have the highest tendency to segregate at W GB. Also, they calculated the mechanical and electronic contribution to the segregation energies using existing predictive continuum models. Despite a large number of detailed studies describing the effect of solute atoms in W GBs, the segregation energies are mostly explained in terms of atomic size effects; none of them considered the role of electron contribution of solute atoms on the host material. In particular, detailed information about the influence on bond strength and charge transfer between atoms with large differences in their electronegativity is lacking. In the present work, we investigate the segregation behavior of selected *d* elements, namely Ti, Ag and Ta, at different W GB structures. Specifically, we examine both low/high STGB as most of the polycrystalline materials are randomly composed of these two types of STGBs. Moreover, several previous and recent studies [21–23] revealed the strong correlation and energetics and stability and the variation of electronic structure. Thus, the impact of the solute metal atoms on the electronic structure and charge transfer to the surrounding host lattice, in bulk as well as at GBs, is

scrutinized to shed light on the microscopic mechanisms responsible for the structural stabilization/destabilization. Finally, nanocrystalline W-Ag and W-Ta alloys were deposited by magnetron sputtering with a concentration of solute metal of around 10%. The alloys were post-annealed at temperatures of 700 and 900°C for up to 15h in order to observe the segregation tendency of different solute atoms. The high-resolution electron imaging confirms a strong tendency for Ag to segregate, particularly~~especially~~ when annealed at 900°C. Ta is by comparison highly stable upon annealing at elevated temperatures and shows nanometer-size segregated clusters forming only at the grain boundary interfaces.

2. Methodology

2.1 Experimental setup

Thin films of tungsten were deposited by magnetron sputtering in an argon atmosphere on Al_2O_3 and Si substrates. Pure metallic targets were used (i.e. an alloy was prepared by co-deposition from two metallic targets); substrate bias was -50 V. The target power for the targets was selected to produce alloys with 10 at. % of dopant metals (Ag and Ta). To assess the segregation behaviour of the solute atoms, annealing was performed in a vacuum (pressure below 10^{-5} Pa) at temperatures up to 900°C. This study presents the structural and chemical characterisation of the as-deposited and annealed W alloys. The imaging and electron dispersive x-ray spectroscopy (EDX) characterisation were performed using a state-of-the-art JEOL ARM 200F (STEM) and FEI Titan^3 (TEM) electron microscopes equipped with a probe and image aberration corrector and operating at 200 and 300kV acceleration voltage respectively.

2.2 Computational details

The non-spin total energy calculations were performed using density functional theory implemented in the Vienna ab-initio simulation package (VASP) code [24–27]. The interaction between ions and electrons is described by the Projector Augmented Wave (PAW) method

[28]. The exchange-correlation contributions were described by the Perdew-Burke-Ernzerhof (PBE) within the generalized gradient approximation (GGA)[29,30]. The Brillouin zone was sampled using a Monkhorst–Pack scheme[31] and k-point mesh for all STGB are listed in Table.1. The calculated bulk lattice parameter (3.172Å) is slightly higher than the experimental value ~~of~~ 3.1648 Å[32]. The cutoff energy of 450 eV was used in all calculations and the plane wave cutoff and k-point density are both checked for convergence for each system to be within 0.001 eV per atom. All atoms were relaxed until the forces on each of them are less than 0.001eV/Å in our calculations. The segregation energy (E_{seg}) is defined as the difference between the solution energy of solute atom (M= Ti, Ag and Ta) in GB and in bulk[33,34], given by

$$E_{seg} = E_{\mathrm{f}}^{\mathrm{GB,M}} - E_{\mathrm{f}}^{\mathrm{bulk,M}} \quad (1)$$

Here $E_{\mathrm{f}}^{\mathrm{GB,M}}$ and $E_{\mathrm{f}}^{\mathrm{bulk,M}}$ are the formation energy of one solute atom at GB site and in bulk W, respectively. The value of $E_{\mathrm{f}}^{\mathrm{GB,M}}$ is given by

$$E_{\mathrm{f}}^{\mathrm{GB,M}} = E_{\mathrm{GB,M}}^{\mathrm{T}} - E_{\mathrm{GB}}^{\mathrm{T}} + \mu_{\mathrm{W}} - \mu_{\mathrm{M}} \quad (2)$$

$$E_{\mathrm{f}}^{\mathrm{bulk,M}} = E_{\mathrm{bulk,M}}^{\mathrm{T}} - (\mathrm{N}-1)\mu_{\mathrm{W}} - \mu_{\mathrm{M}} \quad (3)$$

Here, $E_{\mathrm{GB,M}}^{\mathrm{T}}$ and $E_{\mathrm{GB}}^{\mathrm{T}}$ are the total energy of the supercell containing GB with/without solute atom M. $E_{\mathrm{bulk,M}}^{\mathrm{T}}$ is the total energy of bulk W containing a solute atom. N, μ_{W} and μ_{M} are the total number of atoms, chemical potential of W and solute M, respectively in their reference structure. For bulk W calculation, 128-atom ($4\times4\times4$) supercell, was used. The value of μ_{M} was determined as the total energies of the respective cells divided by the number of atoms in their reference state, i.e., bcc, hcp, fcc and bcc for W, Ti, Ag and Ta, respectively. More details about system setup for determining μ_{M} is given in Table. 1.

Table. 1. Supercell parameters for bulk W, Ti, Ag and Ta.

setup	No. of atoms	Dimension (Å)	K-points	E cut-off
W(bcc)	128	12.68× 12.68 × 12.68	4×4×4	450
Ti(hcp)	48	9.82× 8.50 ×9.14	4×4×4	520
Ag(fcc)	108	12.48× 12.48 × 12.48	4×4×4	520
Ta(bcc)	128	13.24× 13.24 × 13.24	4×4×4	520

Finally, the amount of charge transfer between different atoms was quantified based on Bader Charge [35] using Bader code [36]. All atomistic visualizations are made using Ovito software [37], while charge densities were visualized using the VESTA software[38].

2.3 GB Models construction

In literature[8,18,19,39], it has been demonstrated that GB segregation exhibits a strong dependence on the intrinsic structure of GBs. In the present study, to investigate the effect of various GBs types on the segregation behavior of solute atoms, six different [001] symmetric tilt GBs were examined. The studied STGBs are $\Sigma145\,(0\bar{1}17)$, $\Sigma61\,(0\bar{1}11)$, $\Sigma65\,(0\bar{1}8)$, $\Sigma13\,(0\bar{1}5)$, $\Sigma5\,(0\bar{1}3)$ and $\Sigma5\,(0\bar{1}2)$. The first three GBs represent models for low-angle STGBs while the last three GBs are examples for high-angle STGBs. These STGB were generated by rotating two identical body-centered cubic (bcc) W grains, with a predefined orientation, around the <100> axis with a desirable tilt angle. The rotational axis is parallel to the GB plane and symmetric tilt boundaries are mirrored about the grain boundary plane. The tilt angle (θ) was varied between 6.4 to 53 degrees. Fig. 1 displays two different types of STGBs, namely, low-angle STGB ($\theta_T < 15^\circ$) and high-angle STGBs ($\theta_T > 15^\circ$). The low-angle STGBs consist of an array of <100> dislocations as described by the dislocation model [40]. While the high-angle STGBs can be described by isolating repeating patterns called basic structural units. For example, $\Sigma5\,(0\bar{1}3)$ and $\Sigma5\,(0\bar{1}2)$ STGBs structures are formed by repeating D and C structural units, respectively.

To avoid high energy GB configurations and obtain minimum energy structure, the first ~~one~~ of the two overlapped atoms within 0.7 Å distance was removed followed by structural optimization.

The generated GBs structure was initially minimized by molecular statics (MS) using the Large-scale Atomic/Molecular Massively Parallel Simulator (LAMMPS)[41]. The Embedded Atom Method interatomic (EAM) potential, referred to as EAM3 in Ref [42], was used to describe the interaction between W atoms. This potential was fit to experimental data to correctly reproduce the physical properties of W such as lattice constant, cohesive energy, surface energy and stacking fault. During MS relaxation, the atoms were allowed to relax in a direction perpendicular on the GB plane. Then, the obtained structure is further minimized via ionic relaxation using DFT~~,~~; further details ~~is~~can be found in supplementary material (section 1). The relaxed structure of different STGBs reveals quite different structural motifs in which one of grains is shifted with respect to another grain leading to a break of mirror symmetry at the interface, as illustrated in Fig. 1. Similar behavior was commonly observed and reported for GBs in bcc metals [43–45]. For example, in the case of the relaxed $\Sigma5\,(0\bar{1}\,3)$ a broken mirror symmetry via a shift of one grain with respect to the other along [100] direction was observed as displayed in Fig. S1 (supplement). Similar behavior was also reported by several previous experimental and theoretical studies [45–47].

Table .2. Summary of STGBs characteristic including type, tilt angle, dimensions in (Å), number of atoms, K-points and GB energies.

Type	Angle	$L_x \times L_y \times L_z$	N	K-points	γ_{GB} (Jm^{-2})
Low-angle STGB					
$\Sigma145\,(0\bar{1}17)$	6.73°	3.172×54.05×12.7	120	5×1×3	1.84
$\Sigma61\,(0\bar{1}11)$	10.38°	3.172×35.04×18.95	124	5×1×3	2.67
$\Sigma65\,(0\bar{1}\,8)$	14.25°	3.172×25.57×18.88	90	5×1×3	2.78
High-angle STGB					
$\Sigma13\,(0\bar{1}\,5)$	22.61°	6.3×16.1×24.28	152	5×2×1	2.27

$\Sigma5(0\bar{1}3)$	36.86°	6.26×9.97×20.9	80	5×3×1	2.18
$\Sigma5(0\bar{1}2)$	53.13°	6.3×14.19×28.04	152	5×3×1	2.73

The GB energy γ_{GB} is determined from the difference in energy between the supercell containing GB and another supercell of an equal number of atoms in the bulk environment, divided by the cross-section of the supercell. Therefore, the GB energy γ_{GB} is given[19]

$$\gamma_{GB} = \frac{E_{GB}^{T} - N\mu_{\mathrm{W}}}{2A} \tag{4}$$

Where E_{GB}^{T} is the total energy of the supercell containing the grain boundary, N is the total number of atoms, μ_{W} chemical potential of W atom in its equilibrium bulk structure and A represents the area of grain boundary plane.

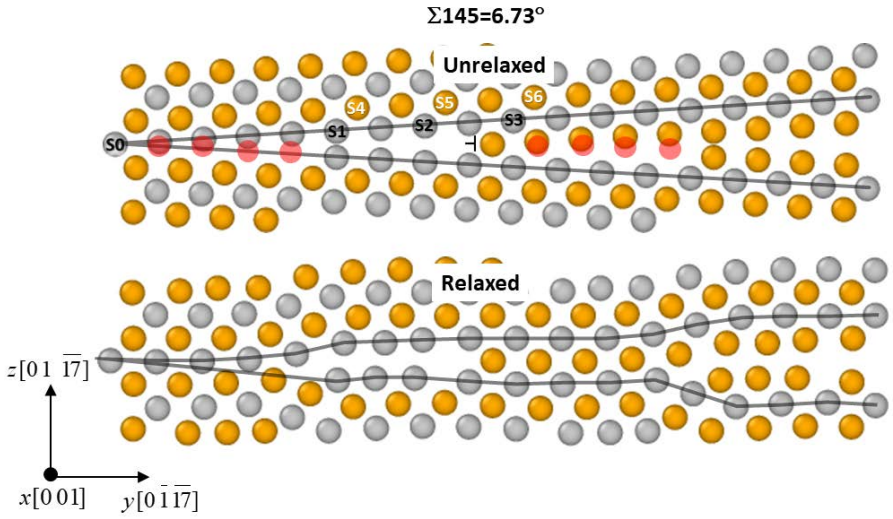

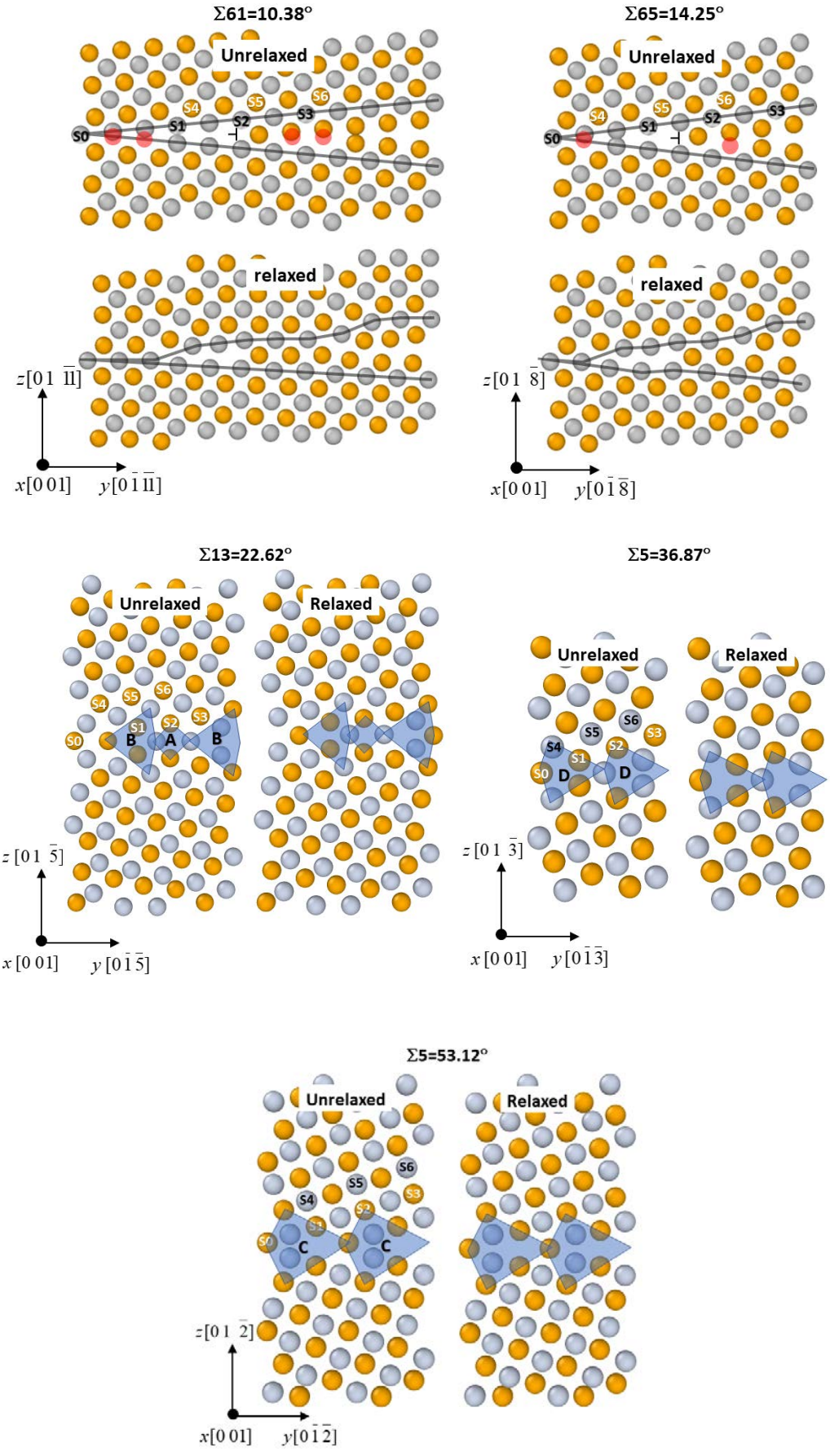
Σ61=10.38°
Unrelaxed
S0
S1
S2
S3
S4
S5
S6
relaxed
z[0 1 11]
x[0 0 1]
y[0 1 11]
Σ65=14.25°
Unrelaxed
S0
S1
S2
S3
S4
S5
S6
relaxed
z[0 1 8]
x[0 0 1]
y[0 1 8]
Σ13=22.62°
Unrelaxed
Relaxed
S0
S1
S2
S3
S4
S5
S6
B
A
B
z [0 1 5]
x [0 0 1]
y [0 1 5]
Σ5=36.87°
Unrelaxed
Relaxed
S0
S1
S2
S3
S4
S5
S6
D
D
z [0 1 3]
x [0 0 1]
y [0 1 3]
Σ5=53.12°
Unrelaxed
Relaxed
S0
S1
S2
S3
S4
S5
S6
C
C
z[0 1 2]
x[0 0 1]
y[0 1 2]

Fig. 1. Different STGBs structures considered in this study, low-angle STGB (left) and high-angle STGBs (right panel). Note that the structure of $\Sigma 13\,(0\bar{1}\,5)$ is represented by mix of A+B structural units, while C and D are structural units for $\Sigma 5\,(0\bar{1}\,2)$ and $\Sigma 5\,(0\bar{1}\,3)$, respectively. In the case of low-angle STGBs their structures can be descried as an array of <100> dislocations.

Also, the excess volume is one of the key factors that determines the segregation of solute atoms; hence, the excess volume of different GB sites located within the grain boundary was estimated using Voronoi analysis [48]. Fig. S5(a) (supplement) shows the distribution of atomic volume for different STGBs. As shown in Fig. S5(a), only STGBs below tilt angle $\theta < 23^{o}$ contain some GB sites having smaller atomic volume, above $\theta > 23^{o}$ all GBs sites have both small/ large atomic volume compared to bulk atomic volume. These GB sites with smaller (larger) atomic volume represent compressed (stretched) sites ~~which~~ that can obstruct (accommodate) solute atoms with different sizes. For the studied STGBs, the largest atomic sites are about 25 % can be observed in $\Sigma 145\,(0\bar{1}17)$ and $\Sigma 13\,(0\bar{1}5)$. Fig. S5(b) (supplement) displays the average (symbols) and range (vertical lines) of atomic volume for six different STGBs considered in this work. Thus, the range of studied STGBs here can be considered, to a first approximation, as representative of general random grain boundaries.

3. Results and Discussion

3.1 Formation and segregation energies of solute atoms

The formation energies of different solute metals in bulk W, calculated by Eq. (3), are -0.78, 2.49 and -0.462 eV for Ti, Ag and Ta, respectively. In the case of STGB, the formation energies of Ag are always positive (endothermic) while the formation energies of both Ti and Ta for most GB site are negative (exothermic). The segregation energy calculated using Eq. (1), profiles of a solute atom at different GBs sites are plotted in Fig. (2). Additional GB sites at the vicinity of GB core have been examined and the data of segregation energies for different solute atoms are listed in Table. S2(supplement).

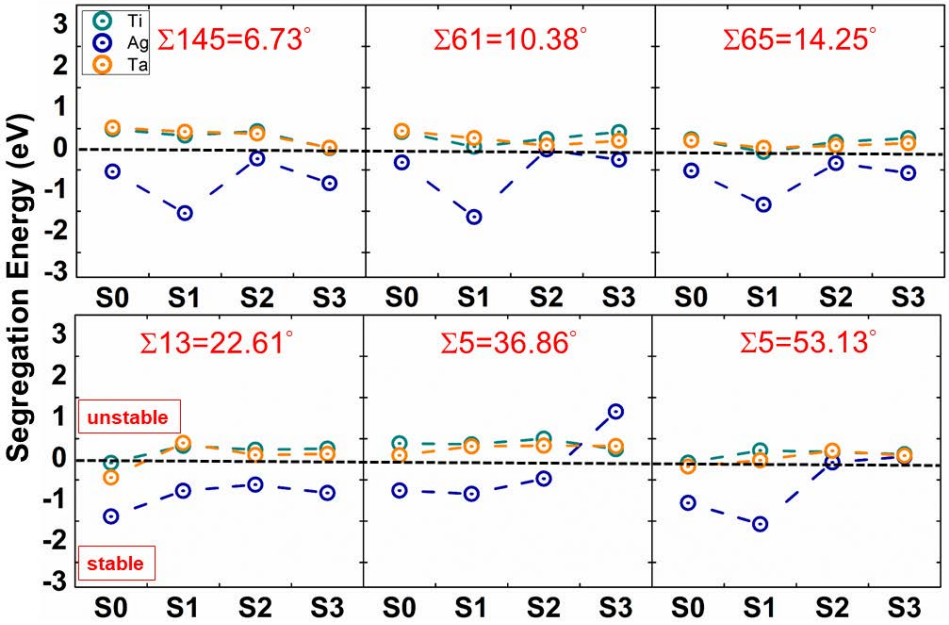

Fig. 2. Segregation energy profile of solute atoms M=Ti, Ag and Ta in low-angle (upper panel) and high-angle (lower panel) STGBs of W.

Fig. 2 shows the segregation energy profiles for solute M in different STGBs of W. It can be seen, for low-angle STGBs, the segregation energy of both Ti and Ta atoms are positive (unstable) implying anti-segregation behavior at these GB sites. Thus, DFT results predict Ti, Ta-depletion in the core and vicinity of GB which is confirmed by TEM observations[14,15]. In contrast, Ag atom tends to segregate to most of GB sites with the most stable position at site S1. In the case of high-angle STGBs, ~~again~~ Ag atoms again retain their behavior of segregation to most of GB sites. For Ti and Ta, they barely exhibit segregation preferences, in particular at core sites S0, for $\Sigma 13\,(0\bar{1}5)$ and $\Sigma 5\,(0\bar{1}2)$, see Fig. 2. From these results, one can conclude that Ag atoms segregate into both the core and the vicinity of GB planes, whereas Ti and Ta atoms are more likely to reside at GB core for only high-angle STGBs. Our finding is supported by recent experimental transmission electron microscopy (TEM) observations in which Ti atoms tend to segregate into GB core of W thins films[14,15]. The highest value of the segregation energy of Ti, Ag and Ta atoms are -0.017, -1.59 and -0.2 eV, respectively. Our DFT results for Ti and Ta in the case of $\Sigma 5\,(0\bar{1}3)$ are in close agreement with recent DFT work by Wu et al[19] as illustrated in Fig. S8 (supplement). Furthermore, similar behavior of Ti and Ta segregation

was observed for $\Sigma 3(112)$ as reported in Refs.[19,20]. Additionally, similar trends were also reported for surface segregation energies of Ti, Ag and Ta in W obtained by DFT in the local density approximation (LDA) by Ruban et al.[49]. In general, we found that the segregation tendency of Ag is independent ~~on~~ of the GB intrinsic as proven by segregation preferences to most of GB sites. In contrast, Ti and Ta exhibit segregation tendency to segregate to S0 only. In the following section, we attempt to investigate each GB site characteristics~~, t~~. Therefore we can then predict the site preference for segregation of different solute atoms.

3.2 Mechanical and electronic contributions to solute segregation energy

It is well established that the physics mechanisms underlying segregation propensity of solute atoms are mainly the elastic strain induced from solute-host size mismatch (mechanical) and bonding state (electronic) at GB site. In literature, several continuum models were developed to predict the segregation energy of solute atoms in the host matrix. It is worth mention ~~here,~~that we have estimated segregation of solute atoms from available predictive continuum models. For instance, we employed McClean model, Eq.(5) in Ref [50], and modified Miedema model Eq.(15) in Ref. [33] to estimate the segregation energy of solute atoms in W.

$$\Delta E_{el}^{seg} = \Delta E_{el} = \frac{24\pi K_A G_B r_B r_A (r_B - r_A)}{3K_A r_A + 4G_B r_B} \quad (5)$$

Where, $K_{A/B}$, $G_{A/B}$ and $r_{A/B}$ are the bulk, shear and atomic radius of host (A) and solute (B), respectively. The experimental value of K and G for Ti, Ag, Ta and W are taken from Refs. [51–53].

$$E_{seg,GB}^{chemical} = \left[1 - \frac{Z_{GB}}{Z_{bulk}}\right]^{1/2} \left[-\Delta H_{sol} - c_0 \gamma_A V_A^{2/3} + c_0 \gamma_B V_B^{2/3}\right] \quad (6)$$

Where Z_{GB} and Z_{bulk} denote the coordination number of the solute atom at grain boundary and bulk, respectively. ΔH_{sol} is the solution enthalpy of solute atom. The second and third terms describe the interfacial driving force for segregation at GBs. c_0 is empirical constants,

γ and V are the surface energy and atomic volume of solute and host at their corresponding pure metals. The last to terms in Eq. (6) can be approximated to the atomisation energy of pure metals. The experimental values of the atomization energies for M=Ti, Ag and Ti were taken from Refs. [54–56]. The predicted results, using Eq. (5) and (6), are listed in Table.3.

Table. 3. The predicted mechanical and electronic contribution to the segregation energy of solute atom in W according to McClean and modified Miedema models.

	$E^{\text{seg}}_{\text{mech}}$ (eV)	E^{seg}_{elect} (eV)
W-Ti	-0.33	-1.57796
W-Ag	-0.55	-1.67018
W-Ta	-0.08	-1.93861

Yet another pure atomistic approach can be used to estimate the mechanical and chemical contribution to the solution energy of solute atom in host matrix [57,58]

$$E^{\text{M}}_{\text{mec}} = E^{\text{rel}}_{\text{tot}}(\text{M@ host}) - E^{\text{un-rel}}_{\text{tot}}(\text{M@ host}) \quad (7)$$

$$E^{\text{M}}_{\text{elect}} = E^{\text{un-rel}}_{\text{tot}}(\text{M@ host}) - E^{\text{rel}}_{\text{tot}}(\text{host}) + E_{\text{W}} - E_{\text{M}} \quad (8)$$

Where $E^{\text{rel}}_{\text{tot}}(\text{M@ host})$, $E^{\text{un-rel}}_{\text{tot}}(\text{M@ host})$ are the total energy of relaxed and unrelaxed structure containing solute atom (M) and $E^{\text{rel}}_{\text{tot}}(\text{host})$ is the total energy of relaxed structure of pure host. It should be pointed that M atom is added to a fully relaxed host W GB; hence $E^{\text{un-rel}}_{\text{tot}}(\text{M@ host})$ in Eq. (7) represents the energy change associated with lattice distortion due to replacing W with M solute at a GB site. In the bulk cases, as listed in Table. 4, for all solute elements, the electronic contribution to solution energy is significantly larger than the mechanical contribution.

Table. 4. The mechanical and electronic contributions, calculated by Eqs. (7) and (8), to the solution energy of segregant (M) in bulk W.

	$E^{\text{M}}_{\text{mec}}$ (eV)	$E^{\text{M}}_{\text{elect}}$ (eV)
W-Ti	-0.02	-0.76
W-Ag	-0.23	2.72
W-Ta	-0.04	-0.42

From Table.3, it can be noticed that the mechanical contribution in the case of Ag is considerably higher in magnitude when compared to Ti and Ta cases. This can be understood since both Ti (160 pm) and Ta (170 pm) have a comparable atomic size to W (162 pm), while Ag (144 pm) has a smaller atomic size than W atom. Also, the positive value of the electronic contribution in the case of Ag indicates that weak chemical interactions between valence electrons of Ag and W atoms.

From Eqs. (7) and (8), on can calculate the segregation tendency (ΔE), defined as the relative solution energy with respect to M inside the bulk, as

$$\Delta E = \left[E^{\mathrm{M}}_{\mathrm{mec}}(\mathrm{M}@\ \mathrm{GB}) - E^{\mathrm{M}}_{\mathrm{mec}}(\mathrm{M}@\ \mathrm{bulk})\right] + \left[E^{\mathrm{M}}_{\mathrm{elect}}(\mathrm{M}@\ \mathrm{GB}) - E^{\mathrm{M}}_{\mathrm{elect}}(\mathrm{M}@\ \mathrm{bulk})\right] \qquad (9)$$

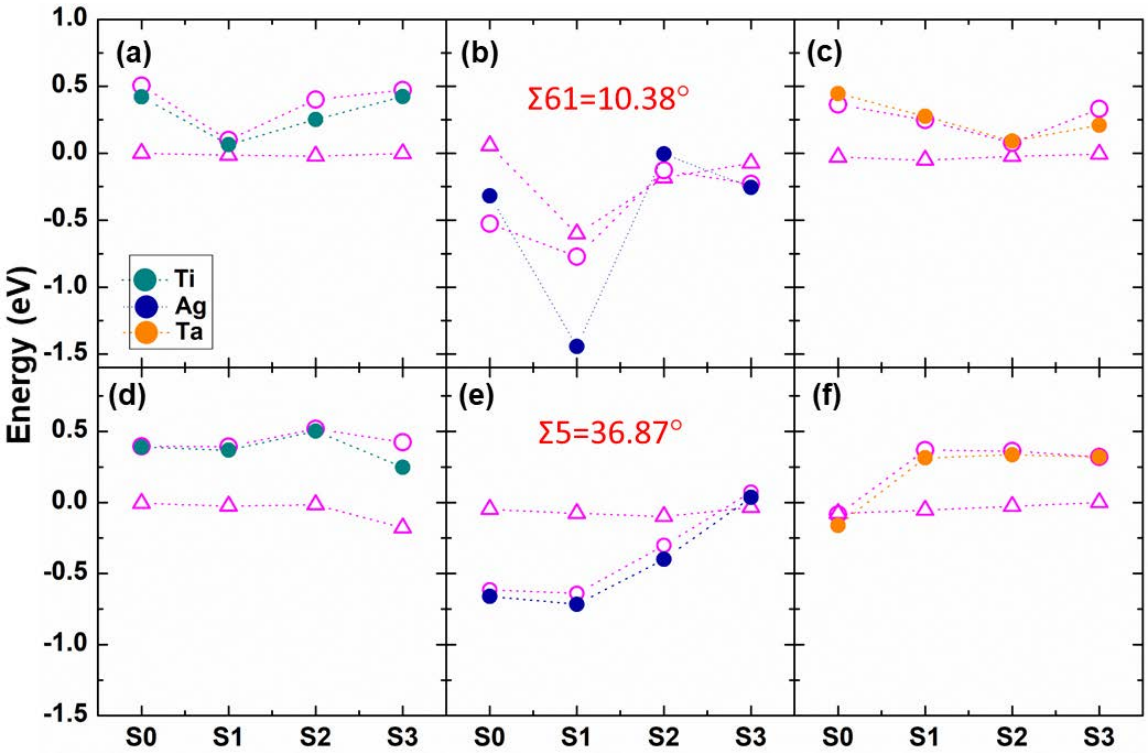

Fig. 3. The mechanical (triangle) and electronic (open circle) contribution (in eV) to the segregation energy as calculated by Eqs. (7-9). The sum of both contributions is also plotted (filled circle). The upper (lower) panel represent Σ61 (Σ5) STGBs.

The change of electronic and mechanical contributions to the segregation energies of solute atoms into different STGBs of W are plotted in Fig. 3. For most of GB sites, the electronic contributions dominate, while the mechanical part is not significant. This behavior is supported by TEM results showing that no large lattice distortion was observed upon adding substitute

atoms indicating they can easily accommodate into host cell. Generally, for low-angle STGBs, the electronic contribution, for most alloying elements at S1, decreases when compared to S0 site and this may be attributed to the increase of the coordination number at S1 site. However, this trend has not been observed in the case of high-angle STGBs. While the McClean model can produce results~~, which are~~ comparable to those obtained by Eq. (7), the Miedema model overestimates the values predicted by DFT. The discrepancies~~,~~ between results obtained by the continuum models and DFT results~~,~~ may be attributed to that some parameters in continuum models are taken from experiments ~~which~~ that were carried out at a finite temperature, while DFT results are obtained at 0K.

Interestingly, for STGBs, we found that the shortest W-M bond length has a minimum value at site S1 except $\Sigma5(0\,\bar{1}2)$ GB where the minimum is located at S2, as shown in Fig. 4. Also, we noticed that the value of these minima, for different solutes, is lower in the case of low-angle STGBs when compared to high-angle STGBs. Also, it is found that the value of these minima continuously decreasing with increasing misorientation angle (θ). From plot, it can be seen that, for most of GB sites, the value of shortest W-M lengths decreases in the following order Ag> Ta > Ti, respectively. From the W-M bond length analysis and Voronoi analysis (Table. S1), one can conclude the following:

As has been illustrated in Fig. 2, for low-angle STGBs, S1 site is the most favorable segregation site for Ag. This site is featured by having the lowest value of shortest W-Ag among all GB sites, larger Voronoi volume, and higher coordination number when compared to S0 site.

On the other hand, the only favorable segregation site, for Ti and Ta, is found at S0 (the core of GB) of both $\Sigma13(0\,\bar{1}5)$ and $\Sigma5(0\,\bar{1}2)$. At this site, two common features were observed, S0 has the largest Voronoi volume among all GB sites, see Table. S3(red numbers), and has the longest W-M bond length, Fig. 4 (d) and (f). This behavior suggests these two oversized

atoms prefer to segregate into open GB (high-angle STGBs) rather than compact interfaces (low-angle STGB).

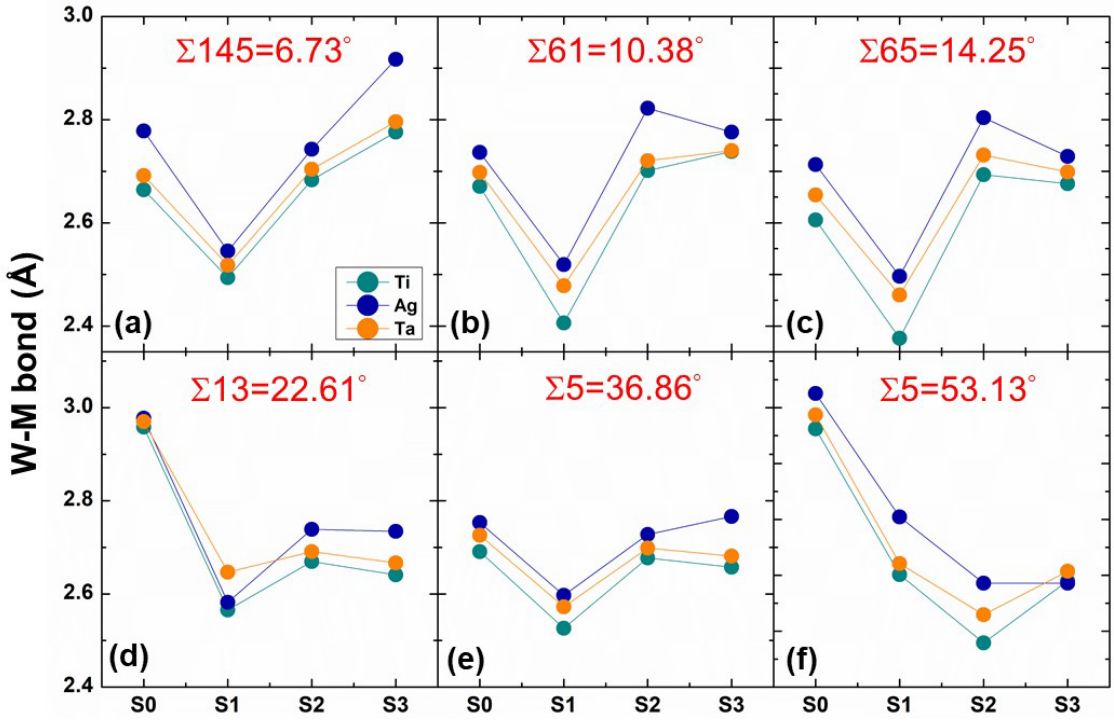

Fig. 4. Shortest bond length between W-M (M=Ti, Ag and Ta) for different STGBs.

From the above discussion, the interplay between atomic volume, coordination and bond length are not sufficient to predict the segregation tendency of M solute atoms in W GBs comprehensively. Therefore, additional factors might be needed to fully describe the segregation preferences at a specific GB site. For instance, it has been shown that the solute–defect binding~~,~~ in bcc refractory metals~~,~~ seems to have strong dependences on the electronic features of solute elements [21]. Thus, in the following section, we will investigate the impact of solute M on the electronic structure of W and its correlation with ~~structure~~ structural stability.

3.3 Effect of solute M=Ti, Ag and Ta on electronic structure of W

We examined the electronic structure variation upon the addition of segregants for both bulk and $\Sigma 5\,(0\,\bar{1}3)$ W, to describe the segregation/anti-segregation behaviour of M= Ti, Ag and Ta at different GBs sites. It is worth pointing out that as d electrons play a major role in determining the physical properties of (TM) elements[22], we will consider only the contributions of d

valence electrons to density of states (DOS). Fig. 5 shows the atom projected density of states (PDOS) for (M=Ti, Ag and Ta atom) and its nearest neighbor atoms in bulk as well as STGBs of W.

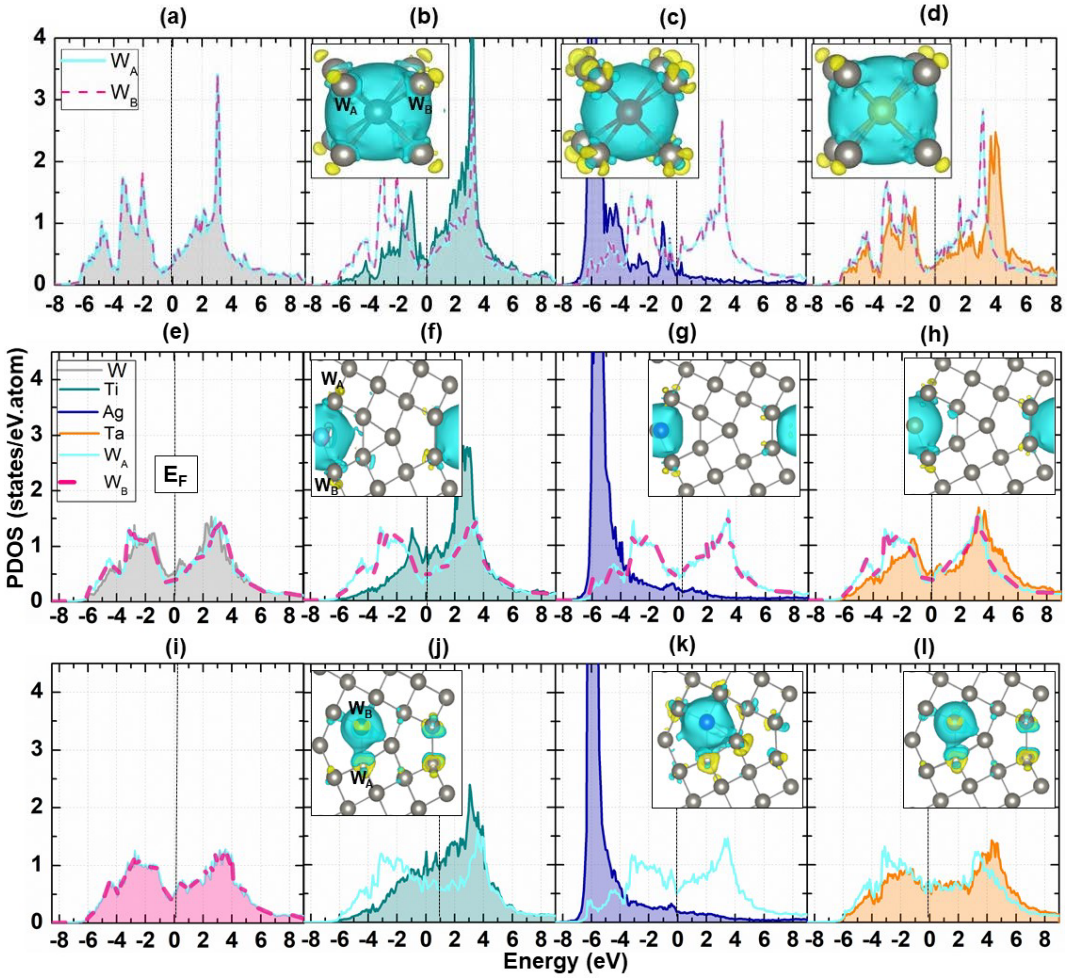

Fig. 5. Atom-projected density of states (PDOS) for the W atoms around M=Ti, Ag and Ta atoms in bulk (a-d) and in $\Sigma 5\,(0\,\bar{1}3)$ STGBs at S0 (e-f) and S1(i-l) sites. Vertical dashed line marks the position of Fermi level at 0 eV energy. Figure insets show the charge transfer between M and neighbouring atoms. The blue (yellow) contours denote loss (gain) charges.

In the case of bulk, PDOS of W is characterized by two sharp peaks around (-1.5 and -3 eV) in the bonding states and a sharp peak in anti-bonding states at 3.6 eV. For Ti atom, most of the $3d$ states are unoccupied, while for Ag atom, the majority of $4d$ electrons are located in occupied states as indicated by the sharp peak, see Fig. 5. This can be understood from the valence electrons configuration of each element where Ag has a completely filled d -band, while Ti, Ta and W have partially filled d-band. The number of d valence electrons of Ti, Ag,

Ta and W are 2, 10, 3 and 4, respectively. Besides, the strong 5 d state hybridization between both W and Ta, as evident by overlapped PDOS Fig. 5(d), indicates strong W-Ta bonding. In contrast, a relatively weak or even no band overlapping was observed for Ti and Ag with W, as shown in Fig.5 (b) and (c). In the case of Ti, d valence electrons are weakly hybridizing with W neighbours in antibonding state. Thus, the origin of bonding in Ti may be due to band filling as evidenced by the increase of PDOS of the two sharp beaks in bonding states and the reduction of the sharp peak in antibonding states compared to bulk W, see Fig.5 (b).

In the case of STGBs, for example $\Sigma5(0\bar{1}3)$, Fig. 5(e-l)~~.~~ shows the PDOS of M atom with its nearest neighbor W atoms. The PDOS curves of clean GB show excellent overlapping between W atoms as illustrated in Figs. 5(e) and (i) and the metallic bond is dominating bonds between W atoms. Moreover, contrary to bulk W, the featured two sharp peaks in the bonding state disappeared~~,~~; thus, a decrease of stability is expected. Like bulk cases, both Ti and Ag PDOS do not show obvious overlapping with neighboring W atoms at sites S0 Fig.5(f) and (g) and S1 Fig. 5(i) and (k). However, the overlapping of d valence electrons between surrounding W atoms remains unaffected. In contrast, the PDOS features of Ta atoms at GB are similar to those of bulk cases where d valence electrons of Ta atom hybridize with neighboring W atoms leading to strong W-Ta bonding, as shown in Fig. 5(h) and (l).

With respect to Ag, similar to the bulk case, no hybridization between d valence electrons and any of its neighboring W atoms is observed as indicated by the absence of overlapping between their PDOS curves. However, the PDOS of curves W atoms coincides with each other at sites S0 and S1. Therefore, the presence of Ag atom does not affect the stability of the local environment around it. See Fig. 5 (g) and (k).

Besides the above analysis of PDOS of W and solute atoms, we performed Hartigan's dip test to quantify the variation of bimodal shape of W atom and its correlation to the W-M interaction energy (details in supplement section 4). The results of Hartigan's dip test for $\Sigma5(0\bar{1}3)$, Fig.

S7 (supplement), clearly indicate that W atom at GBs sites with less bimodal shape are preferred to be substituted with M atoms having higher d electrons than W in accordance with bond-order potential theory. The results of dip test analysis are consistent with our DFT results in which Ag (more d electron) has a ~~substantial~~ higher tendency than Ti and Ta (lower d electron) to segregate into GB sites of $\Sigma5(0\bar{1}3)$.

The odd behavior of Ag can be understood in terms of $s-d$ compensation hypothesis as reported in Ref. [59]. According to this hypothesis, when filled d band elements alloyed with partially or half-filled elements, an increase in s-electron count is attended by a decrease in d. In Ag case, the valence electronic configurations of Ag and W are $4d^{10}5s^{1}$ and $5d^{4}6s^{2}$, respectively. As the d band of Ag is completely filled as the same as s band of W, then it is anticipated one electron from a partially filled d band of W transfer to s band of Ag. We have plotted the PDOS for Ag and W in both bulk as well as STGBs cases, see Fig. 6. Excellent $s-$ electron hybridization is observed between Ag with its nearest neighbor W atom as indicated by strong overlapping, see Fig. 6. Moreover, compared to bulk case, two features from PDOS of neighbor W atom are observed~~,~~. ~~f~~Firstly; the peak at (3.1 eV) vanishes in antibonding states and, secondly~~;~~, the peak (around -6.1 eV) in bonding states ~~are~~ is enhanced. The above analysis of PDOS graphs supports the substantial GB segregation tendency of Ag in W host.

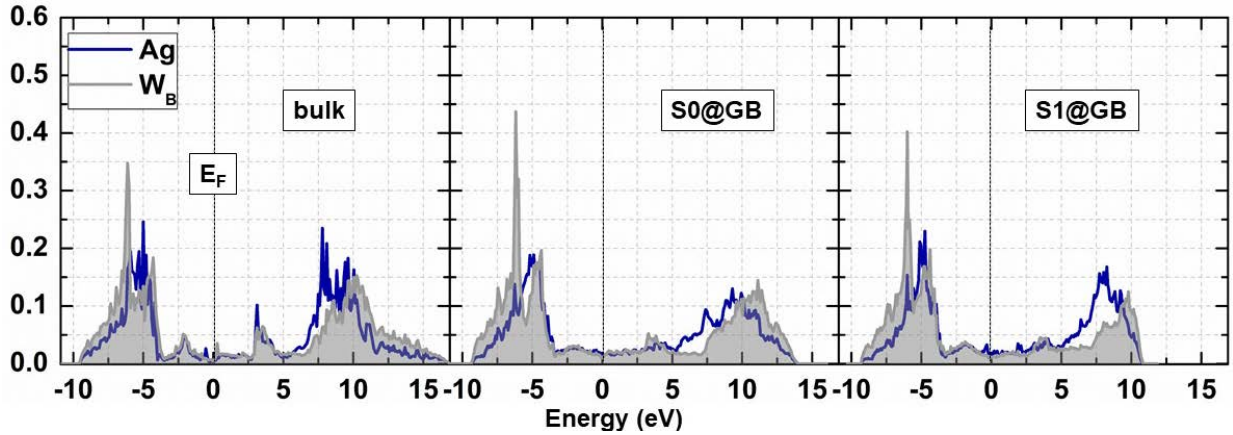

Fig. 6. Atom-projected density of states (PDOS) for the s-electron of Ag and its nearest neighbor W in bulk as well as at different GB sites in $\Sigma5(0\bar{1}3)$ STGBs. Vertical dashed line marks the position of Fermi level at 0 eV energy.

Furthermore, the nature of bonding between solute and host atoms can be evaluated by the change of valence charge due to charge transfer among atoms with different electronegativity. The electronegativity values of Ti, Ag, Ta and W atoms are 1.54, 1.93, 1.5 and 2.36, respectively; hence the charge transfer from M to W atom is expected. The valence charge difference ($\Delta\rho$), defined as the difference between the charge density of a compound and its constituent, given by

$$\Delta\rho = \rho_{W-M} - \rho_W - \rho_M \quad (10)$$

Where ρ_{W-M} is the valence charge density of a supercell containing W and one solute atom M, ρ_W and ρ_M are valence charge densities of a supercell with only W or M, respectively. From Fig. 5 (Inset), both Ti and Ta lose their valence electron charge to their nearest neighbor W atoms, while Ag atom gains more electron charge from surrounding W atoms. To quantify the loss/gain of charge, Bader's analysis was employed, and the results are listed in Tables. (S3) and (S4) (supplement). In the case of bulk, as expected, both Ti and Ta lose nearly equal amount (because of similar electronegativity) of their electron charge to each of 8 first nearest neighbor (1^{st} nn) W atoms. In contrast to Ti and Ta, Ag atom always gains electron charge from each of its neighboring W atoms either in bulk or STGBs.

3.4 Correlation between charge density and bond length

It has been shown in the previous section that bonding between impurity and host atom may be associated with overlapping between their PDOS curves as in the case of Ta. While in the case of Ag and Ti no obvious d valence electrons hybridization with W atoms was shown. Thus, the bonding in these two cases might be discussed in other forms than overlapping. Here we employ charge density and its correlation to bond length to provide further insights on the stability of solute atom in bulk and GB host. Fig. 7 shows the charge density in pure and impurity containing bulk W.

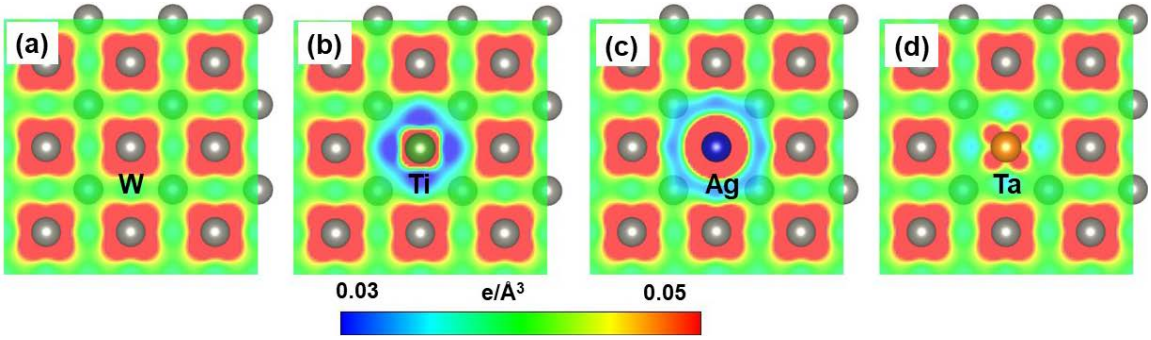

Fig. 7. Charge density distribution around solute atom in bulk W along (100) plane. (a) pure W and W containing (b) Ti, (c) Ag, and (d) Ta.

In pure bulk W, the charge density is uniformly distributed around W atoms as shown in Fig. 7 (a). Adding solute atom to the host may alter the charge density, accumulation/depletion. As illustrated in Fig 7(c), a uniform spherical charge density around Ag with a significant reduction of charge density in the region between Ag and its 1st and 2nd nearest neighbor W atoms lead to weakening bonds between neighboring W atoms. In contrast, the charge accumulation around Ti and Ta atom is small with anisotropic character as illustrated in Fig 7(b) and (d). This anisotropic nature results in an increase in the bond strength between W-M atoms, in particular for $3d$-$5d$ compounds [60]. In order to discuss further details about segregation tendency at different GB sites, we will investigate ~~the~~ the variation of charge density and bond length in the case of $\Sigma5\,(0\,\bar{1}3)$. The obtained results by Bader's analysis are listed in Tables. S3 and S4 (supplement)

Fig. 8 shows the charge density distribution in pure W GB and when W atom is replaced by Ag at S0 and S1 sites. The charge is symmetrically distributed on top and bottom grains with dense charge accumulation between W4-W5(represents the shortest bond length) atom indicating strong bonding. When the W1 atom is replaced by Ag, Fig. 8(b), the charge density is spherically distributed around the Ag atom and associated with a notable reduction of charge density between W-Ag atoms leading to weakening of W4-W5 bond as indicated by the increase of bond length by about 0.02 Å. On the other hand, replacing the W4 atom with Ag

atom causes weakening all W- Ag bonds as indicated by increasing of W-Ag bonds (W2-Ag, W6-Ag, W5-Ag). However, a slight increase in the stability of surrounding W-W bonds (W3-W5 and W5-W6) is observed and illustrated in Fig. 8(c). This behavior explains the increase of substantial segregation tendency of Ag atom to segregate at site S1 compared to S0 site.

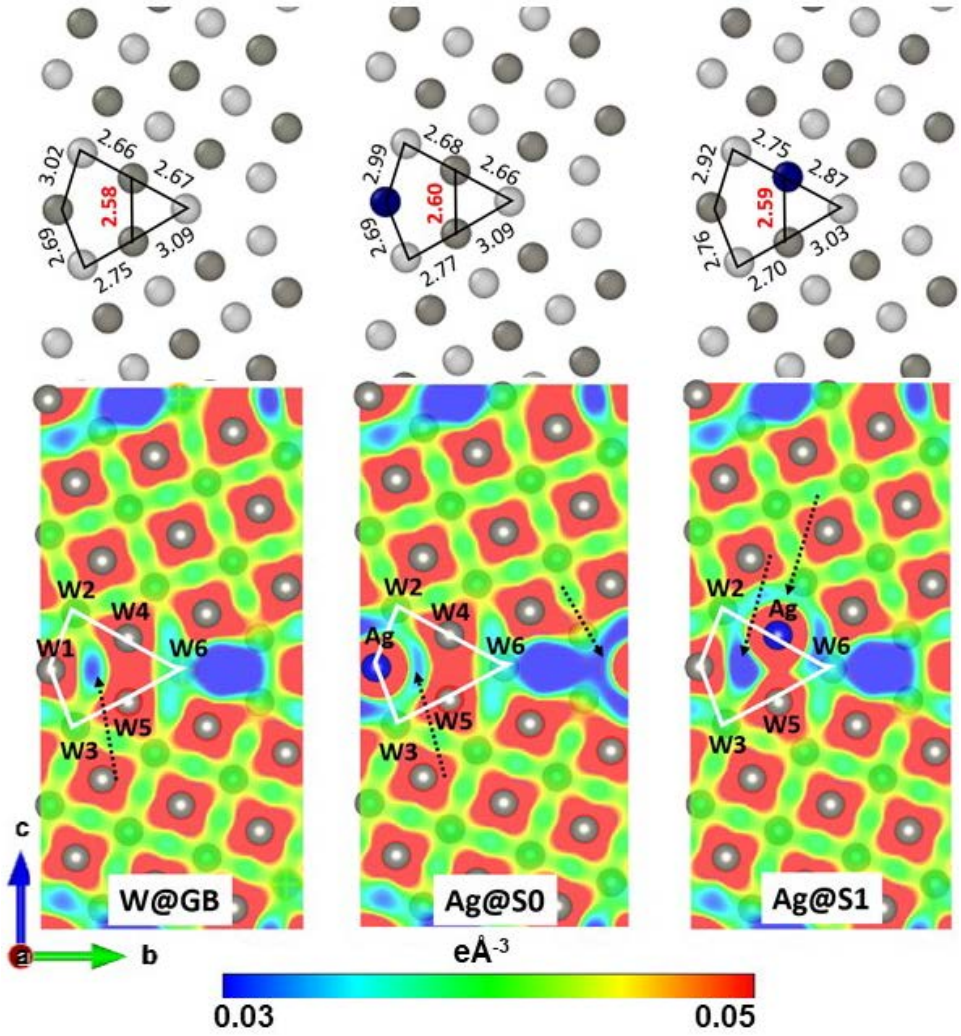

Fig. 8. Bond length analysis results (upper panel) and corresponding charge density distribution along (100) plane for $\Sigma 5(0\bar{1}3)$ STGB (a) clean, (b) with Ag solute at S0 and (c) with Ag solute at S1. Dotted arrows point to regions having different charge densities.

In contrast, replacing W4 atom with Ti atom was found to enhance the bonding at the interface as indicated by the decrease of bond length of Ti-W5 by about 5%, see Fig. S10 (supplement). Besides, the bonding between connecting W atoms strengthened, for instance, W3-W5 and W5-W6 bonds as shown in Fig. 8(b). From Bader's analysis, it is found that, at this site, Ti

atom transfers about 46% of its total charge to neighboring W atoms. On the other hand, when Ta replaces W4, the value of Ta-W5 bond is slightly reduced by only 1% and Ta atom transfers about 32% of its total charge to neighboring W atoms. The loss of valence charge from Ti and Ta in the case of STGB is comparable or even slightly lower than the corresponding value in the bulk case. Thus, ~~causing~~ a reduction of stability of bonds around Ti atom~~,~~ lead~~sing~~ to ~~a~~ higher formation energy at the GB and consequently positive segregation energy.

4. Experimental study on W doped with Ag and Ta

4.1 As-deposited W-Ag and W-Ta

W-Ag and W-Ta films have a thickness of around 1 μm and do not exhibit any significant roughness or structural defects at the microscale. Fig. 9 (b) and (c) show~~s~~ a selected region near the surface of the samples, which confirms the general tendency of the film to grow in well-defined columns. The lateral grain (column) size varies anywhere between 20 and 200 nm.

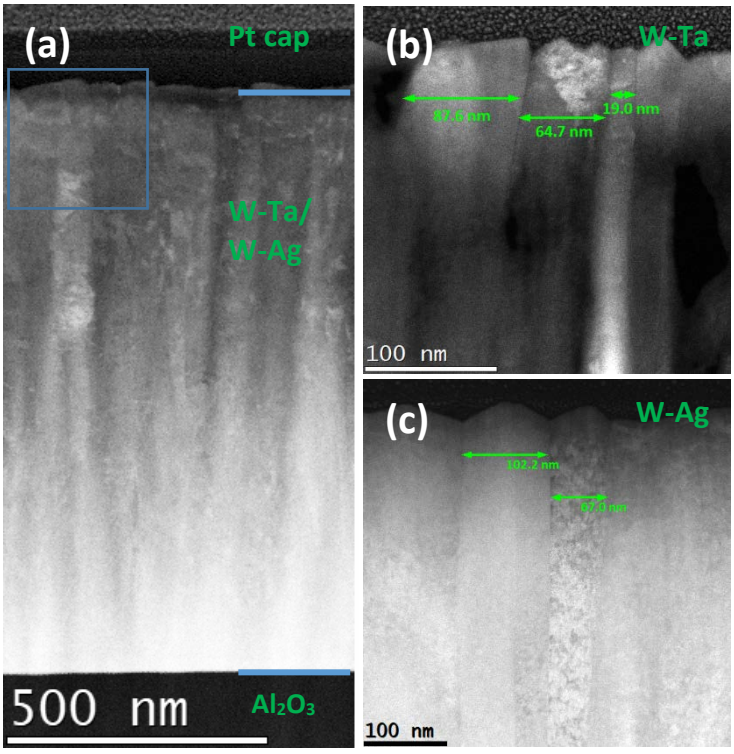

Fig. 9. (a) Low magnification annular dark field (ADF) image of the W-Ta/W-Ag film deposited on Al_2O_3 substrate. High magnification columnar structure near the top interface of (b) W-Ta and (c) W-Ag.

Fig. 10 shows high resolution (HR) images of the columnar structure and neighboring crystallites separated by high-angle tilt grain boundaries (TGB). The difference in orientation arises from the in-plane relative rotation of the adjacent grains. A variety of high and low-angle tilt grain boundaries are observed for the Ta and Ag doped W films.

The solute atoms are easily integrated into the W host unit cell; hence there is no distortion of the lattice or phase separation for the as-deposited films. EDX analysis (not shown) confirms the uniform distribution of the dopants in the solid solution at a concentration of 10 at. % for both W-Ag and W-Ta. Considering the microstructural features and the atomic structure of the two samples, no clear differentiation can be made between the W-based alloys.

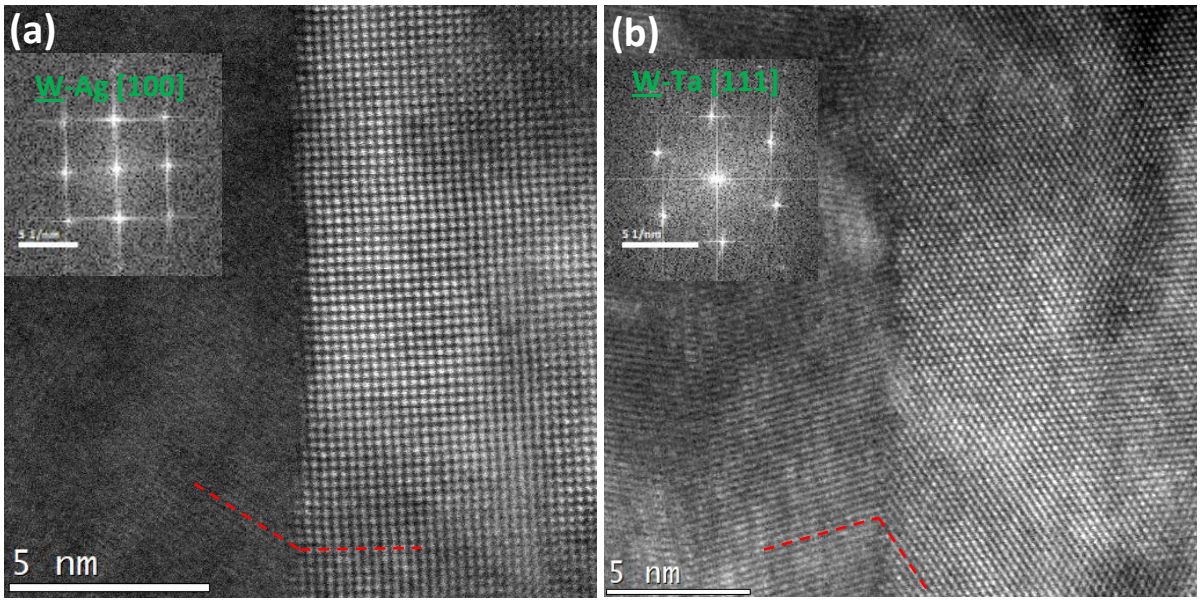

Fig. 10. HR images of neighbouring grains and associated high-angle tilt GBs in (a) W-Ag and (b) W-Ta.

4.2 Post-annealed W-Ag and W-Ta

To study the segregation of solute metals, the doped W thin films were post-annealed initially at 700°C for 15h. No changes occurred to the microstructure of the films and the lateral grain size remained constant. Fig. 11 shows the early stages of dopant metal atom segregation which occurs in both alloys. The main difference between the samples stems from the size and number of dopant-rich islands found at the grain boundaries. As shown in Fig. 11 (a), multiple Ag-rich islands with lateral sizes of up to 10 nm are visible along high-tilt columnar grain boundaries of W-Ag. The W-Ta solid solution is more stable and Ta-rich areas are rarely observed along high-tilt grain boundary planes; they are very small with lateral sizes of 1 nm as shown in

Figure 11 (b). We can conclude here that Ag segregates more easily as shown by the calculations performed on the formation and segregation energy.

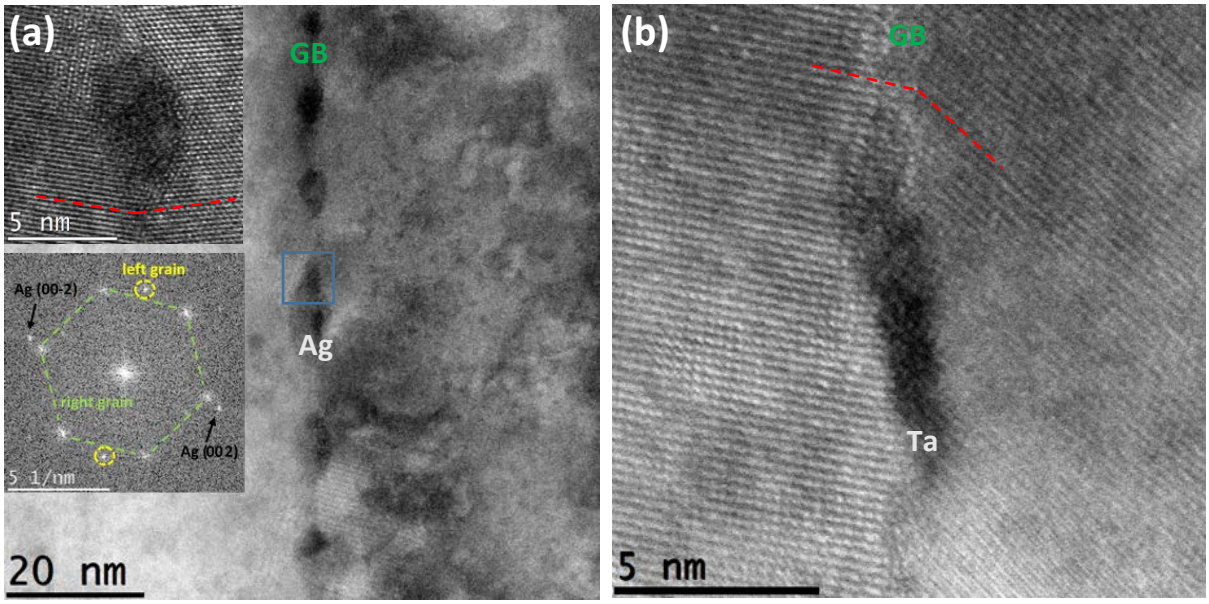

Fig. 11. Evidence of segregation in (a) W-Ag and (b) W-Ta annealed at 700°C.

The post-annealing temperature was increased to 900°C for 15h to accelerate the segregation of both Ag and Ta atoms in the W alloys. As shown in Fig. 12, W-Ag shows considerable phase separation and precipitation along the grain boundaries and within the bulk of the crystallites with Ag-rich regions measuring over 100 nm in length, up to a 10-fold increase when compared to the sample annealed at 700°C. The annealing process causes Ag to separate completely from the W alloy and to form nanometre-sized grains around the Ag-rich regions, see EDX mapping Figs. S12 and S13 (supplement). By comparison, the Ta rich areas in W-Ta increase in lateral size by a factor of three, reaching dimensions of up to 15 nm. Our experiments, together with previous studies on W-Ti sputtered alloys [14,15]), support well the key finding of DFT simulations: Ag is more prone to segregation leading to severe precipitation when compared to Ti or Ta. It should be pointed to the formation of nanoprecipitates of Ag and Ta at GB as illustrated in TEM results Figs. (11) and (12). To explore the tendency of Ag and Ta to form nanometer precipitation at GB, we have calculated the migration energy barrier, using nudged elastic band method, of solute atom in bulk W (details in supplementary section 9). We found

that both Ag and Ta have the lowest migration energy, consequently their propensity to precipitate at GBs as confirmed by TEM results in Fig. 13.

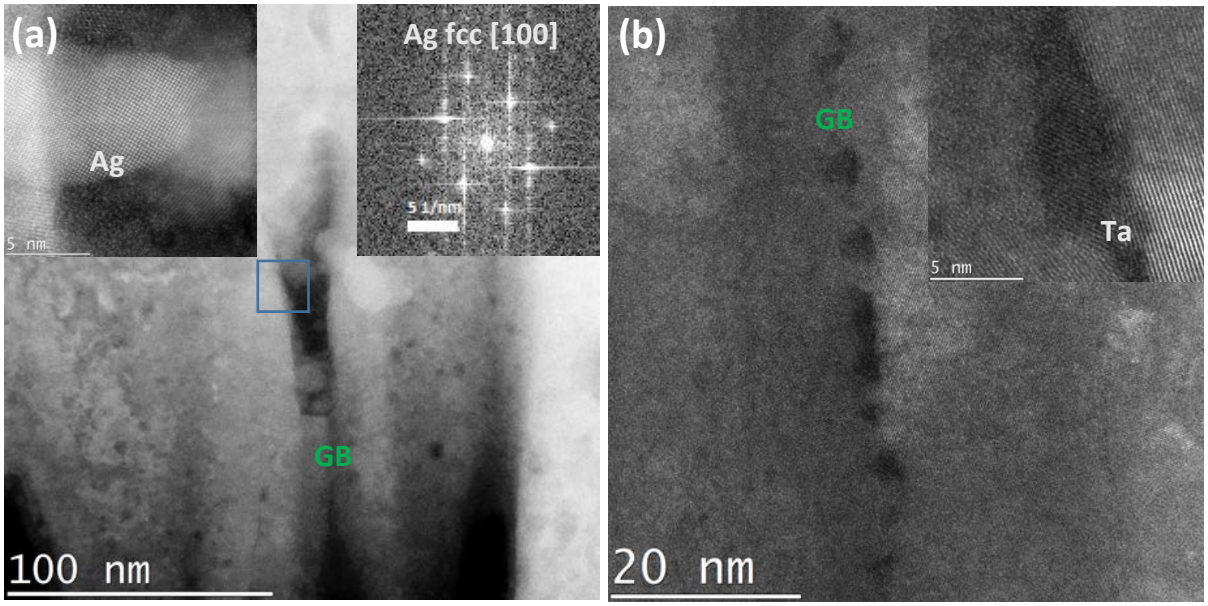

Fig. 12. Annealing at 900°C for 15h: (a) large, precipitated areas and phase separation in W-Ag; (b) nanometer-sized Ta rich islands forming at the GB in W-Ta.

4. Conclusion

The segregation tendency of Ti, Ag and Ta at different low-high STGBs of W was examined using systematic DFT calculations and supported by experiment. Based on GB characteristics, Ti and Ta atoms barely segregate into the core site of $\Sigma 13\,(0\bar{1}\,5)$ and $\Sigma 5\,(0\bar{1}2)$ STGBs while Ag shows substantial segregation tendencies to most of the GB sites in all STGBs. Such behavior is supported by TEM imaging of annealed sputtered alloys and in the case of W-Ag, post annealing at 900°C causes obvious phase separation and precipitation of the solid solution. The decomposition of solution energy revealed that the lattice distortion is not only the driving force for segregation, but it is largely due to electronic contribution. Both bond nature and d valence electrons hybridization play a key role in the stability of solute atoms at GBs. For example, the lower segregation of Ta is ascribed to strong $d-d$ hybridization between W-Ta atom in bulk as well as at GBs while the covalence nature of bonding between Ti-W atoms

leads to a similar result for Ti at W GBs. In the case of Ag, no $d-d$ hybridization was observed for bonds between W and Ag; however, the strong $s-s$ hybridization resulted from $s-d$ compensation is responsible for substantial segregation of Ag. Our DFT results suggest that not only d valence electrons but also $S-$ electrons may play a vital role in bonding between W and Ag. Finally, the obtained results suggest that the electronic contributions should be included in predictive models to ~~get~~ provide accurate and full description of segregation propensity of solute atom in host matrix.

Acknowledgment

The work was supported by EPSRC through the project EP/R041768/1. The authors acknowledge the use of the IRIDIS High Performance Computing Facility, and associated support services at the University of Southampton, in the completion of this work. The electron imaging was performed with the support of the South of England Analytical Electron Microscope (EP/K040375/1), within the David Cockayne Centre for Electron Microscopy, Department of Materials, University of Oxford, and at CEITEC Nano Research Infrastructure (ID LM2015041, MEYS CR, 2016–2019).

References

[1] S. Wurster, N. Baluc, M. Battabyal, T. Crosby, J. Du, C. García-Rosales, A. Hasegawa, A. Hoffmann, A. Kimura, H. Kurishita, R.J. Kurtz, H. Li, S. Noh, J. Reiser, J. Riesch, M. Rieth, W. Setyawan, M. Walter, J.-H. You, R. Pippan, Recent progress in R&D on tungsten alloys for divertor structural and plasma facing materials, J. Nucl. Mater. 442 (2013) S181–S189. https://doi.org/10.1016/j.jnucmat.2013.02.074.

[2] M. Rieth, J.L. Boutard, S.L. Dudarev, T. Ahlgren, S. Antusch, N. Baluc, M.-F. Barthe, C.S. Becquart, L. Ciupinski, J.B. Correia, C. Domain, J. Fikar, E. Fortuna, C.-C. Fu, E. Gaganidze, T.L. Galán, C. García-Rosales, B. Gludovatz, H. Greuner, K. Heinola, N.

Holstein, N. Juslin, F. Koch, W. Krauss, K.J. Kurzydlowski, J. Linke, Ch. Linsmeier, N. Luzginova, H. Maier, M.S. Martínez, J.M. Missiaen, M. Muhammed, A. Muñoz, M. Muzyk, K. Nordlund, D. Nguyen-Manh, P. Norajitra, J. Opschoor, G. Pintsuk, R. Pippan, G. Ritz, L. Romaner, D. Rupp, R. Schäublin, J. Schlosser, I. Uytdenhouwen, J.G. van der Laan, L. Veleva, L. Ventelon, S. Wahlberg, F. Willaime, S. Wurster, M.A. Yar, Review on the EFDA programme on tungsten materials technology and science, J. Nucl. Mater. 417 (2011) 463–467. https://doi.org/10.1016/j.jnucmat.2011.01.075.

[3] J. Ast, M. Göken, K. Durst, Size-dependent fracture toughness of tungsten, Acta Mater. 138 (2017) 198–211. https://doi.org/10.1016/j.actamat.2017.07.030.

[4] J.R. Trelewicz, C.A. Schuh, Grain boundary segregation and thermodynamically stable binary nanocrystalline alloys, Phys. Rev. B. 79 (2009). https://doi.org/10.1103/PhysRevB.79.094112.

[5] T. Chookajorn, H.A. Murdoch, C.A. Schuh, Design of Stable Nanocrystalline Alloys, Science. 337 (2012) 951–954. https://doi.org/10.1126/science.1224737.

[6] A.J. Detor, C.A. Schuh, Microstructural evolution during the heat treatment of nanocrystalline alloys, J. Mater. Res. 22 (2007) 3233–3248. https://doi.org/10.1557/JMR.2007.0403.

[7] K.A. Darling, B.K. VanLeeuwen, J.E. Semones, C.C. Koch, R.O. Scattergood, L.J. Kecskes, S.N. Mathaudhu, Stabilized nanocrystalline iron-based alloys: Guiding efforts in alloy selection, Mater. Sci. Eng. A. 528 (2011) 4365–4371. https://doi.org/10.1016/j.msea.2011.02.080.

[8] P. Wynblatt, D. Chatain, Anisotropy of segregation at grain boundaries and surfaces, Metall. Mater. Trans. A. 37 (2006) 2595–2620. https://doi.org/10.1007/BF02586096.

[9] W.T. Geng, A.J. Freeman, R. Wu, C.B. Geller, J.E. Raynolds, Embrittling and strengthening effects of hydrogen, boron, and phosphorus on a $\ensuremath{\Sigma}5$

nickel grain boundary, Phys. Rev. B. 60 (1999) 7149–7155. https://doi.org/10.1103/PhysRevB.60.7149.

[10] H. Zhou, S. Jin, Y. Zhang, G. Lu, First-principles study of carbon effects in a tungsten grain boundary: site preference, segregation and strengthening, Sci. China Phys. Mech. Astron. 54 (2011) 2164–2169. https://doi.org/10.1007/s11433-011-4495-6.

[11] D. Ma, M. Friák, J. von Pezold, D. Raabe, J. Neugebauer, Ab initioidentified design principles of solid-solution strengthening in Al, Sci. Technol. Adv. Mater. 14 (2013) 025001. https://doi.org/10.1088/1468-6996/14/2/025001.

[12] M. Všianská, M. Šob, The effect of segregated sp-impurities on grain-boundary and surface structure, magnetism and embrittlement in nickel, Prog. Mater. Sci. 56 (2011) 817–840. https://doi.org/10.1016/j.pmatsci.2011.01.008.

[13] P. Lejček, M. Všianská, M. Šob, Recent trends and open questions in grain boundary segregation, J. Mater. Res. 33 (2018) 2647–2660. https://doi.org/10.1557/jmr.2018.230.

[14] O.K. Donaldson, K. Hattar, T. Kaub, G.B. Thompson, J.R. Trelewicz, Solute stabilization of nanocrystalline tungsten against abnormal grain growth, J. Mater. Res. 33 (2018) 68–80. https://doi.org/10.1557/jmr.2017.296.

[15] M. Callisti, F.D. Tichelaar, T. Polcar, In situ TEM observations on the structural evolution of a nanocrystalline W-Ti alloy at elevated temperatures, J. Alloys Compd. 749 (2018) 1000–1008. https://doi.org/10.1016/j.jallcom.2018.03.335.

[16] M. Muzyk, D. Nguyen-Manh, K.J. Kurzydłowski, N.L. Baluc, S.L. Dudarev, Phase stability, point defects, and elastic properties of W-V and W-Ta alloys, Phys. Rev. B. 84 (2011) 104115. https://doi.org/10.1103/PhysRevB.84.104115.

[17] D. Jiang, Q. Wang, W. Hu, Z. Wei, J. Tong, H. Wan, The effect of tantalum (Ta) doping on mechanical properties of tungsten (W): A first-principles study, J. Mater. Res. 31 (2016) 3401–3408. https://doi.org/10.1557/jmr.2016.358.

[18] Z.-W. Li, X.-S. Kong, C.-S. Liu, Q.-F. Fang, Segregation of alloying atoms at a tilt symmetric grain boundary in tungsten and their strengthening and embrittling effects, Chin. Phys. B. 23 (2014) 106107. https://doi.org/10.1088/1674-1056/23/10/106107.

[19] X. Wu, Y.-W. You, X.-S. Kong, J.-L. Chen, G.-N. Luo, G.-H. Lu, C.S. Liu, Z. Wang, First-principles determination of grain boundary strengthening in tungsten: Dependence on grain boundary structure and metallic radius of solute, Acta Mater. 120 (2016) 315–326. https://doi.org/10.1016/j.actamat.2016.08.048.

[20] D. Scheiber, R. Pippan, P. Puschnig, A. Ruban, L. Romaner, Ab-initio search for cohesion-enhancing solute elements at grain boundaries in molybdenum and tungsten, Int. J. Refract. Met. Hard Mater. 60 (2016) 75–81. https://doi.org/10.1016/j.ijrmhm.2016.07.003.

[21] Y.-J. Hu, G. Zhao, B. Zhang, C. Yang, M. Zhang, Z.-K. Liu, X. Qian, L. Qi, Local electronic descriptors for solute-defect interactions in bcc refractory metals, Nat. Commun. 10 (2019) 4484. https://doi.org/10.1038/s41467-019-12452-7.

[22] Z. Xu, S. Tanaka, M. Kohyama, Grain-boundary segregation of 3d-transition metal solutes in bcc Fe: ab initio local-energy and d-electron behavior analysis, J. Phys. Condens. Matter. 31 (2019) 115001. https://doi.org/10.1088/1361-648X/aafd00.

[23] J.-X. Shang, X.-D. Zhao, F.-H. Wang, C.-Y. Wang, H.-B. Xu, Effects of Co and Cr on bcc Fe grain boundaries cohesion from first-principles study, Comput. Mater. Sci. 38 (2006) 217–222. https://doi.org/10.1016/j.commatsci.2006.02.010.

[24] G. Kresse, J. Hafner, Ab initio molecular dynamics for liquid metals, Phys. Rev. B. 47 (1993) 558–561. https://doi.org/10.1103/PhysRevB.47.558.

[25] G. Kresse, J. Hafner, Ab initio molecular-dynamics simulation of the liquid-metal--amorphous-semiconductor transition in germanium, Phys. Rev. B. 49 (1994) 14251–14269. https://doi.org/10.1103/PhysRevB.49.14251.

[26] G. Kresse, J. Furthmüller, Efficiency of ab-initio total energy calculations for metals and semiconductors using a plane-wave basis set, Comput. Mater. Sci. 6 (1996) 15–50. https://doi.org/10.1016/0927-0256(96)00008-0.

[27] G. Kresse, J. Furthmüller, Efficient iterative schemes for ab initio total-energy calculations using a plane-wave basis set, Phys. Rev. B. 54 (1996) 11169–11186. https://doi.org/10.1103/PhysRevB.54.11169.

[28] P.E. Blöchl, Projector augmented-wave method, Phys. Rev. B. 50 (1994) 17953–17979. https://doi.org/10.1103/PhysRevB.50.17953.

[29] J.P. Perdew, J.A. Chevary, S.H. Vosko, K.A. Jackson, M.R. Pederson, D.J. Singh, C. Fiolhais, Atoms, molecules, solids, and surfaces: Applications of the generalized gradient approximation for exchange and correlation, Phys. Rev. B. 46 (1992) 6671–6687. https://doi.org/10.1103/PhysRevB.46.6671.

[30] J.P. Perdew, J.A. Chevary, S.H. Vosko, K.A. Jackson, M.R. Pederson, D.J. Singh, C. Fiolhais, Erratum: Atoms, molecules, solids, and surfaces: Applications of the generalized gradient approximation for exchange and correlation, Phys. Rev. B. 48 (1993) 4978–4978. https://doi.org/10.1103/PhysRevB.48.4978.2.

[31] H.J. Monkhorst, J.D. Pack, Special points for Brillouin-zone integrations, Phys. Rev. B. 13 (1976) 5188–5192. https://doi.org/10.1103/PhysRevB.13.5188.

[32] Atomic Defects in Metals / Atomare Fehlstellen in Metallen | H. Ullmaier | Springer, (n.d.). https://www.springer.com/gp/book/9783540514350 (accessed October 28, 2020).

[33] V.I. Razumovskiy, S.V. Divinski, L. Romaner, Solute segregation in Cu: DFT vs. Experiment, Acta Mater. 147 (2018) 122–132. https://doi.org/10.1016/j.actamat.2018.01.011.

[34] D. Zhao, Y. Li, Lattice distortion induced site dependent carbon gettering at twin boundaries in silicon, J. Alloys Compd. 712 (2017) 599–604. https://doi.org/10.1016/j.jallcom.2017.04.111.

[35] R.F.W. Bader, A quantum theory of molecular structure and its applications, Chem. Rev. 91 (1991) 893–928. https://doi.org/10.1021/cr00005a013.

[36] W. Tang, E. Sanville, G. Henkelman, A grid-based Bader analysis algorithm without lattice bias, J. Phys. Condens. Matter. 21 (2009) 084204. https://doi.org/10.1088/0953-8984/21/8/084204.

[37] A. Stukowski, Visualization and analysis of atomistic simulation data with OVITO–the Open Visualization Tool, Model. Simul. Mater. Sci. Eng. 18 (2009) 015012. https://doi.org/10.1088/0965-0393/18/1/015012.

[38] K. Momma, F. Izumi, VESTA 3 for three-dimensional visualization of crystal, volumetric and morphology data, J. Appl. Crystallogr. 44 (2011) 1272–1276. https://doi.org/10.1107/S0021889811038970.

[39] J. Wang, R. Janisch, G.K.H. Madsen, R. Drautz, First-principles study of carbon segregation in bcc iron symmetrical tilt grain boundaries, Acta Mater. 115 (2016) 259–268. https://doi.org/10.1016/j.actamat.2016.04.058.

[40] W.T. Read, W. Shockley, Dislocation Models of Crystal Grain Boundaries, Phys. Rev. 78 (1950) 275–289. https://doi.org/10.1103/PhysRev.78.275.

[41] S. Plimpton, Fast Parallel Algorithms for Short-Range Molecular Dynamics, J. Comput. Phys. 117 (1995) 1–19. https://doi.org/10.1006/jcph.1995.1039.

[42] M.-C. Marinica, L. Ventelon, M.R. Gilbert, L. Proville, S.L. Dudarev, J. Marian, G. Bencteux, F. Willaime, Interatomic potentials for modelling radiation defects and dislocations in tungsten, J. Phys. Condens. Matter. 25 (2013) 395502. https://doi.org/10.1088/0953-8984/25/39/395502.

[43] W. Setyawan, R.J. Kurtz, Ab initio study of H, He, Li and Be impurity effect in tungsten ${upSigma, J. Phys.: Condens. Matter. 26 (2014) 135004. https://doi.org/10.1088/0953-8984/26/13/135004.

[44] R. Janisch, C. Elsässer, Segregated light elements at grain boundaries in niobium and molybdenum, Phys. Rev. B. 67 (2003) 224101. https://doi.org/10.1103/PhysRevB.67.224101.

[45] T. Ochs, O. Beck, C. Elsässer, B. Meyer, Symmetrical tilt grain boundaries in body-centred cubic transition metals: An ab initio local-density-functional study, Philos. Mag. A. 80 (2000) 351–372. https://doi.org/10.1080/01418610008212057.

[46] G.H. Campbell, M. Kumar, W.E. King, J. Belak, J.A. Moriarty, S.M. Foiles, The rigid-body displacement observed at the $\sum = 5$, (310)-[001] symmetric tilt grain boundary in central transition bcc metals, Philos. Mag. A. 82 (2002) 1573–1594. https://doi.org/10.1080/01418610208240038.

[47] M. Wojdyr, S. Khalil, Y. Liu, I. Szlufarska, Energetics and structure of<001> tilt grain boundaries in SiC, Model. Simul. Mater. Sci. Eng. 18 (2010) 075009. https://doi.org/10.1088/0965-0393/18/7/075009.

[48] F. Aurenhammer, Voronoi Diagrams—a Survey of a Fundamental Geometric Data Structure, ACM Comput Surv. 23 (1991) 345–405. https://doi.org/10.1145/116873.116880.

[49] A.V. Ruban, H.L. Skriver, J.K. Nørskov, Surface segregation energies in transition-metal alloys, Phys. Rev. B. 59 (1999) 15990–16000. https://doi.org/10.1103/PhysRevB.59.15990.

[50] H.A. Murdoch, C.A. Schuh, Estimation of grain boundary segregation enthalpy and its role in stable nanocrystalline alloy design, Prof Schuh Angie Locknar. (2013). https://dspace.mit.edu/handle/1721.1/80352 (accessed June 25, 2019).

[51] G. Simmons, Single crystal elastic constants and calculated aggregate properties: a handbook, 2d ed., Cambridge, Mass., M.I.T. Press, 1971.

[52] F.H. Featherston, J.R. Neighbours, Elastic Constants of Tantalum, Tungsten, and Molybdenum, Phys. Rev. 130 (1963) 1324–1333. https://doi.org/10.1103/PhysRev.130.1324.

[53] K. Skotnicová, V.M. Kirillova, O.I. Zaporozhets, J. Drápala, I. Szurman, Investigation of physical properties of tungsten-based single crystals using an ultrasonic method, in: 2014.

[54] Metals Reference Book 5th Edition by Smithells Colin - AbeBooks, (n.d.). https://www.abebooks.co.uk/book-search/title/metals-reference-book-5th-edition/author/smithells-colin/ (accessed August 21, 2019).

[55] Introduction to Solid State Physics 6th edition by Kittel, Charles (1986) Hardcover, 6 edition, John Wiley & Sons, n.d.

[56] P. Janthon, S. (Andy) Luo, S.M. Kozlov, F. Viñes, J. Limtrakul, D.G. Truhlar, F. Illas, Bulk Properties of Transition Metals: A Challenge for the Design of Universal Density Functionals, J. Chem. Theory Comput. 10 (2014) 3832–3839. https://doi.org/10.1021/ct500532v.

[57] R. Wu, A.J. Freeman, G.B. Olson, First Principles Determination of the Effects of Phosphorus and Boron on Iron Grain Boundary Cohesion, Science. 265 (1994) 376–380. https://doi.org/10.1126/science.265.5170.376.

[58] W.T. Geng, A.J. Freeman, G.B. Olson, Influence of alloying additions on grain boundary cohesion of transition metals: First-principles determination and its phenomenological extension, Phys. Rev. B. 63 (2001) 165415. https://doi.org/10.1103/PhysRevB.63.165415.

[59] R.E. Watson, M. Weinert, G.W. Fernando, Charge transfer in transition-metal alloying: Charge-tailing effects, Phys. Rev. B. 43 (1991) 1446–1454. https://doi.org/10.1103/PhysRevB.43.1446.

[60] L.G. Wang, A. Zunger, Why are the 3d-5d compounds CuAu and NiPt stable, whereas the 3d-4d compounds CuAg and NiPd are not, Phys. Rev. B. 67 (2003) 092103. https://doi.org/10.1103/PhysRevB.67.092103.